

Wide-Swath Ocean Altimetry Using Radar Interferometry

Ernesto Rodríguez, Brian D. Pollard, Jan M. Martin,

Jet Propulsion Laboratory
California Institute of Technology
Pasadena, CA
E-mail: er@vermeer.jpl.nasa.gov

submitted to
IEEE Transactions on Geoscience and Remote Sensing
July, 1999

Abstract

The sampling limitations of a single nadir-looking ocean altimeter have long been known, and multiple altimeter missions and bistatic altimeter configurations have been proposed as solutions. In this paper we suggest an alternate method that overcomes the sampling issue through the combined use of nadir-looking altimetry and off-nadir radar interferometry. This technique can achieve nearly complete global coverage with sufficient resolution to map mesoscale ocean features. We first present a conceptual mission design, and examine in detail the error budgets for such an interferometric system. Secondly, we overcome the stringent spacecraft attitude knowledge requirements for such a system by introducing two new techniques that use the nadir altimeter data to remove attitude and phase errors. Finally, we simulate the expected accuracy of the system with TOPEX/Poseidon data and an eddy-resolving ocean circulation model, and present a sample instrument that can provide the accuracy and resolution necessary to map mesoscale ocean phenomena.

1 Introduction

The last decade has seen a dramatic demonstration of the measurement capabilities of nadir-looking ocean altimeters. As a preeminent example, the NASA/CNES TOPEX/Poseidon altimeter has provided unprecedented views of the development of the El Niño phenomenon [1] and discovered unsuspected properties of ocean Rossby waves [2], among many other observations.

However, due to the requirement that large-scale ocean circulation be adequately sampled temporally while avoiding aliasing due to tidal signals, the full spatial spectrum of ocean variability cannot be observed using this type of system. The TOPEX/Poseidon orbit, for instance, has equatorial gaps of close to 300 km, which are significantly larger than the typical size of an ocean eddy.

This limitation of nadir-looking altimeters has long been recognized, and several solutions have been proposed, including multi-altimeter missions [3] [4], multi-beam altimeters [5], and bistatic altimeter configurations [6]. In this paper, we present a new measurement concept to address the mesoscale sampling problem: a wide-swath coherent interferometer combined with a nadir looking altimeter, and a self-calibration process to remove systematic errors.

The proposed system bears similarities with the multi-beam altimeter proposed by Bush et al. [5], but introduces key improvements to render the implementation of such a system feasible. The following list briefly summarizes these improvements:

- Two new techniques are introduced that use the nadir altimeter and the interferometer data to remove interferometric baseline tilt and phase errors. In the past such errors have made the interferometric technique infeasible due to the stringent requirements placed on the interferometric baseline metrology system.
- Completely coherent Maximum Likelihood digital on-board processing allows for the optimal utilization of the phase, and removes height biases due to angular variations in the ocean radar cross section.
- Short synthetic aperture processing is used to reduce spatial decorrelation effects, improve height noise performance, and reduce antenna length requirements.
- Full-swath processing allows for a nearly continuous map of sea surface height variation.

Using such a system, we show that nearly complete global spatial coverage can be achieved with a single platform, without sacrificing temporal resolution. This provides an attractive alternative to the other multiple platform solutions which have been proposed [3], [4], [6], including a large improvement in spatio-temporal resolution.

The plan of this paper is as follows. In section 2, we review the sampling required to measure a variety of ocean features, and briefly discuss the capabilities of current and other proposed altimeter systems. Section 3 describes our measurement concept and contrasts it against proposed alternatives. In the following section, we examine the measurement error sources and derive the sensitivity equations for our proposed system. The key step in making the interferometric measurement feasible lies in the ability to use the data itself to remove systematic errors due to baseline tilts: in section 5, we describe two calibration techniques and derive expected calibration accuracies. Finally, in section 6 we present a design which meets the mesoscale eddy measurement requirements, together with a full measurement error budget. We also discuss design trade-off considerations for the implementation of the wide-swath altimeter concept.

2 Oceanographic Sampling Requirements

The ocean circulation exhibits a wide range of features with varying temporal and spatial scales. Table 1 [7] summarizes the most prominent ocean circulation signatures and their associated temporal, spatial, and height scales. Past altimeter missions, most notably TOPEX/Poseidon (T/P), have concentrated on studying large scale circulation phenomena, which can be characterized roughly as having spatial scales which are a substantial fraction of the ocean basin, and height signatures from a few centimeters to a few tens of centimeters.

The spatial resolution requirements for large scale oceanographic signals, and other applications such as long-term sea level rise, are not very stringent (sampling on the order of 100 km or coarser), but the height accuracies required are quite stringent, with a goal of centimeter level absolute accuracy. The temporal sampling of energetic phenomena, such as boundary currents, and also the requirement to avoid tidal aliasing [8], make repeat pass orbits with periods on the order of ten days highly desirable.

Ocean mesoscale eddies have a much stronger height signature, thus requiring reduced height accuracy for their measurement, but have much smaller spatial scales as well as short time scales. While it is possible to sample large scale oceanographic signals adequately with a single altimeter system, it is impossible to sample simultaneously both the spatial and temporal characteristics of mesoscale ocean eddies. For example, in order to obtain a ten-day repeat orbit, T/P must accept an equatorial track spacing of about 300 km, while characteristic eddy scales at these latitudes are closer to 100 km–150 km [9]. Eddy sizes, which are proportional to the Rossby radius of deformation, decrease with latitude, so they also may be missed at mid-latitudes even though the altimeter track separation also decreases with latitude. Although significant work has been done in studying ocean mesoscale characteristics and eddy momentum fluxes (see [10] and [9] for two

prominent examples), global characterization and monitoring of the mesoscale eddy field cannot be accomplished with a single altimeter.

An additional limitation of a nadir-looking altimeter is its limited ability to measure the geostrophic current vector. Using the geostrophic equations [11], the altimeter height measurements result only in an estimate of the geostrophic velocity component in the direction perpendicular to the altimeter track. Direct measurements of the full, two-dimensional geostrophic currents can only be obtained at the orbit cross-over points, limiting the ability to calculate directly global and regional mass and energy fluxes.

The sampling limits of a single, nadir-looking altimeter can be improved by combining multiple altimeter missions, as proposed in [4] and [3], among others. Fig. 1 [12] presents the space-time resolution capabilities for a variety of satellite combinations together with the typical scales of globally observed mesoscale eddies. It is clear from this figure that in order to sample adequately the mesoscale eddy spectrum, a minimum of three properly coordinated nadir-looking altimeters is required.

In the remainder of this paper, we present a single-platform concept which addresses the above requirements of high accuracy nadir altimetry together with a high (~ 14 km) resolution, wide-swath (~ 200 km), two-dimensional global ocean height map every ten days. The space-time sampling characteristics of such a wide-swath altimeter system are shown in Fig. 1, and represent a substantial improvement over the multiple-platform concept.

3 Measurement Concept

From the discussion in the previous section, it is evident that the only means by which a single platform can simultaneously meet the space and time sampling requirements for all oceanographic signals of interest is by going beyond the traditional narrow swath altimeter concept to a side-looking wide swath system. Elachi et al. [13] examine the performance characteristics of a scanning altimeter system and conclude that system accuracy is limited by three factors: 1) pulse spreading due to the finite antenna aperture; 2) unknown variations in the radar cross section over the radar footprint; and, 3) errors due to insufficient knowledge of the spacecraft roll angle.

Unlike nadir-looking altimeters, the return waveform from a side-looking beam does not exhibit a sharp leading edge, and the accuracy with which the mean height can be tracked is governed by the accuracy with which the centroid of the return radar pulse (or a similar measure) can be determined. For side looking systems, the accuracy with which the centroid can be tracked is proportional to the number of samples in the return (i.e., the radar bandwidth) and inversely proportional to the pulse spreading, which is inversely proportional to the antenna dimension in

the cross-track direction. An ingenious method of obtaining large effective apertures and multiple antenna beams while using only two smaller antennas is proposed by Bush et al. [5]. In their scheme, the return signals from the two antennas are coherently differenced and normalized by the total return power to generate multiple interferometric lobes, each of which can be thought as being due to an antenna of dimensions equivalent to the separation between the two smaller antennas. Height estimation is accomplished by tracking the energy in individual interferometric fringes.

While this proposal solves the antenna dimension problem, it still suffers from the limitations in accuracy due to roll errors, which we discuss at length in the following sections, and the cross-section angular variations, which shift the energy centroid of each interferometric fringe. The radar cross section, and its angular variations, are a function of wind speed and direction, as well as attenuation due to clouds. The challenge of correctly predicting the angular and spatial variation of the cross section from the altimeter data alone with an accuracy sufficient for obtaining centimeter level height accuracy is daunting, and probably impossible to meet, given our current state of understanding.

The problem of cross-section angular variations in the previous approach, which we call “amplitude” interferometry, can be overcome if we use the interferometric phase alone to measure topography, independent of the signal amplitude [14] [15]. We briefly summarize this “phase” interferometry approach in the following paragraphs.

In the phase interferometry technique, the relative phase Φ between signals from the same point arriving at the two interferometric antennas can be converted to an estimate of the look angle, θ , to that point by means of the interferometric equation (see Fig. 2)

$$\Phi = k(r_1 - r_0) \quad (1)$$

where $k = 2\pi/\lambda$ is the electromagnetic wavenumber, r_0 is the range from the reference antenna to the surface, and r_1 is the range to the second interferometric antenna. After some geometry, one can show that the look angle can be obtained from the interferometric phase by the equation

$$\sin(\theta - \alpha) = \frac{\Phi}{kB} \left[1 - \frac{1}{2} \frac{B}{r_0} \frac{\Phi}{kB} \right] - \frac{1}{2} \frac{B}{r_0} \quad (2)$$

$$\approx \frac{\Phi}{kB} \quad (3)$$

where B is the length of the interferometric baseline, and α is the angle of the baseline relative to the tangent plane.

Given the look direction θ , the surface height, h , and cross-track position, x , relative to a tangent plane at the center of the swath is given by

$$h = H - r_0 \cos \theta \quad (4)$$

$$x = r_0 \sin \theta \quad (5)$$

where H is the platform height above the tangent plane. (The geolocation equations relative to the spherical Earth can be easily derived, but we use the tangent plane as a reference since it simplifies the resulting expressions. A simple conversion can be applied to go between the two coordinate systems.)

These equations fully specify both the height and location of each individual resolution cell within the radar swath, not just of the entire interferometric fringe, as in the amplitude interferometry technique. Since, as we shall see below, the maximum likelihood estimator for the interferometric phase is formed so that the mean result (although not the measurement noise) is independent of the signal amplitude, the height bias due to cross section variations is not present in this technique, again in contrast to the amplitude interferometry approach.

To satisfy the ocean sampling and accuracy requirements for both mesoscale and large-scale oceanography, we propose a joint altimeter-interferometer system with the following characteristics (see Fig. 3):

- An orbit similar to that of T/P to optimize temporal sampling and reduce tidal aliasing: 1336 km altitude, 66° inclination, and a ten-day repeat period.
- A dual frequency (Ku and C-band) nadir-looking altimeter system, similar to the T/P system to provide centimeter level accuracy large scale oceanographic measurements and cross-calibration for the interferometric system.
- A dual-swath interferometric system providing coverage on either side of the nadir system. The interferometric swaths extend from 15 km to 100 km in the cross-track direction, providing a total instrument swath of 200 km. To reduce height noise, we average in the along and cross-track directions to produce a final data product with a 14 km spatial resolution, or about half of the minimum Rossby radius of deformation. This resolution should be sufficient for mapping eddies at all latitudes, and can be degraded at lower latitudes (where eddies are larger) to reduce measurement noise, if desired.
- A three-frequency radiometer system similar to the one used in T/P for providing nadir tropospheric delay measurements. The correction of tropospheric (and ionospheric) delays for the off-nadir data is discussed below.

The 200 km swath gives nearly complete global coverage. Fig. 4 summarizes the instrument spatial coverage as a function of latitude, and compares with the coverage obtained by the T/P instrument, assuming a two-kilometer nadir swath. As can be seen from this figure, the wide-swath instrument provides full spatial coverage at higher latitudes, with some gaps near the equator. To further examine the coverage characteristics near the equatorial region, we present in Fig. 5 a coverage map superimposed on a simulated eddy field obtained from an eddy resolving circulation model [16] [17]. Note that data gaps are typically smaller than eddy scales at these latitudes.

A major difference between the interferometric system we propose here and traditional Interferometric Synthetic Aperture Radar (IFSAR) is that the resolution required for oceanographic applications is much coarser than that obtained by SAR techniques. This implies that full synthetic aperture processing is not required, thus significantly reducing the total computation load. We propose a simple onboard processing system consisting of presumming a few pulses to form a very short synthetic aperture, followed by range compression, and interferogram formation with incoherent interferogram averaging of range pixels to reduce phase noise (see Fig. 6). Only a simple shift (without interpolation) is made to coregister the data sets from the two radar channels. As we see below, due to the limited angular variation and low range resolution, the resulting misregistration error plays a negligible part in the total error budget. This processing can be performed onboard and the resulting average interferogram downlinked at a rate comparable to the nadir altimeter data. This scheme reduces the number of computations and the total data volume by many orders of magnitude relative to conventional SAR data.

The spatial resolution considerations are quite different between the phase and amplitude approaches: in the range direction, the intrinsic resolution for the phase system is determined by the system bandwidth. For the amplitude approach, on the other hand, the range resolution of the measurement is determined by the fringe size, which can be substantially greater than the intrinsic range resolution. In practice, the individual phase measurements can be noisy, and improved accuracy can be obtained by averaging heights in the range direction, at the expense of resolution.

In the along-track direction, on the other hand, both approaches have a spatial resolution limited by the size of the along-track antenna beamwidth, and the along-track averaging time.

4 Measurement Errors

Given the extraordinary precision required for the ocean topography measurement, it is imperative that the error characteristics of any altimetric system be fully characterized. In this section, we present a detailed discussion of each of the error sources affecting the interferometric measurement, and the calibration requirements for a useful ocean measurement system. As we shall see, some

of the error sources need to be known with a precision beyond the capability of current metrology systems. The calibration of these error sources is achieved by using the nadir-looking altimeter, and is described in the Section 5. The nadir altimeter error budget has been examined in detail in the past, and is not addressed here.

Equations (4), (5), and (2) form a complete set of equations for obtaining the position and height of the image point. Examination of these equations shows that there are five sources of error:

1. Height errors due to platform height uncertainty.
2. Errors due to lack of knowledge of the interferometric roll angle, α .
3. Errors due to lack of knowledge of the interferometric baseline, B .
4. Random and systematic errors in the measurement of the interferometric phase, Φ .
5. Errors in the translation between the radar timing measurement to the geometric range, r_0 .

In the following subsections, we examine the characteristics of each error term in detail.

4.1 Systematic Errors

The effect of platform height errors, δH , on measured height is obtained from (4)

$$\delta h = \delta H . \tag{6}$$

The platform height errors are typically dominated by orbit error. Given GPS tracking and precision orbit reconstruction, as in the TOPEX/Poseidon system, height accuracies on the order of a few centimeters can be achieved [18].

Differentiating (4) and (2) with respect to the baseline roll angle α , one finds that an error in the baseline roll $\delta\alpha$ induces a tilt error on the estimated height, as one expects intuitively:

$$\delta h = r_0 \sin \theta \delta \alpha \tag{7}$$

$$= x \delta \alpha . \tag{8}$$

Due to the long range for spaceborne instruments, the requirement on the baseline roll knowledge is very stringent. As an example, a 1 arcsec baseline roll error translates into a 48 cm error at a cross-track distance of 100 km. Therefore, to obtain centimetric accuracy, the baseline roll must be known to within at least 0.1 arcsec. This level of accuracy is currently beyond the capabilities of the best star trackers. The next section discusses how this parameter may be calibrated using the nadir altimeter and cross-over adjustments.

The effect of a baseline dilation error δB is obtained by similar differentiation:

$$\delta h = -r_0 \sin \theta \tan(\theta - \alpha) \frac{\delta B}{B} . \quad (9)$$

For our application, this term is of secondary importance for three reasons: first, composite materials can be manufactured which exhibit extremely small unmodellable fraction expansion errors; second, the error is quadratically dependent on the incidence angle, rather than linear; and third, the geometric factors are much smaller than for the roll error, given the small incidence angles in the proposed design.

The effect of a phase error $\delta \Phi$ is given by

$$\delta h = r_0 \frac{\sin \theta}{kB \cos(\theta - \alpha)} \delta \Phi . \quad (10)$$

Given the small incidence angle regime used for the proposed instrument, the angular variation of this error is practically identical to the baseline roll error, and the two terms can be combined into an effective roll error. As with the roll error, the calibration requirements on the interferometric phase are very stringent: to achieve centimetric accuracy, the non-random component of the differential phase must be known to an accuracy on the order of 0.1° , which, again, is probably beyond the current state of spaceborne technology. Since both phase and roll errors produce nearly identical height errors, we henceforth speak only of roll errors, but understand that both roll and phase errors are included. Systematic phase errors can be calibrated simultaneously with roll errors using the technique presented in Section 5. In addition to systematic phase errors, thermal noise and radar speckle give rise to random interferometric phase variations. These are examined in the next subsection.

Finally, errors in translating the system timing measurement to a range result in height errors described by the equation

$$\delta h = -\cos \theta \delta r_0 . \quad (11)$$

While system timing is a minor contributor to this error, propagation delays through the troposphere and the ionosphere are significant contributors, as well as scattering effects, such as the Electromagnetic Bias [19]. The magnitude and frequency characteristics of these errors are discussed further below. However, it should be noticed that since θ is so small, the nature of these errors is nearly identical with their contribution to conventional nadir altimetry.

4.2 Random Error Model

As discussed in Section 3, one of the major differences between the concept presented here and the multi-beam altimeter of Bush et al. [5] is the use of coherent interferometric processing, which

fully utilizes the interferometric phase. It is shown in [15] that the Maximum Likelihood (ML) Estimator for the interferometric phase is given by

$$\hat{\Phi} = \arctan \left[\frac{\text{Im}(\sum_{i=1}^{N_L} v_i^{(1)} v_i^{(2)*})}{\text{Re}(\sum_{i=1}^{N_L} v_i^{(1)} v_i^{(2)*})} \right] \quad (12)$$

where $v^{(1)}$ and $v^{(2)}$ denote the return coherent signal at the reference or secondary interferometric channel, respectively. The summation is taken over the interferometric looks; i.e., the independent observations of a given resolution cell with common mean interferometric phase. Given ML estimation, the phase standard deviation, σ_{Φ} , is given by

$$\sigma_{\Phi} = \frac{1}{\sqrt{2N_L}} \frac{\sqrt{1-\gamma^2}}{\gamma} \quad (13)$$

where γ is the correlation coefficient between the two interferometric channels:

$$\gamma = \frac{|\langle v^{(1)} v^{(2)*} \rangle|}{\sqrt{\langle v^{(1)} v^{(1)*} \rangle \langle v^{(2)} v^{(2)*} \rangle}} \quad (14)$$

and $\langle \rangle$ denotes ensemble averaging over speckle realizations.

Equation (13) shows that the phase standard deviation can be predicted if the correlation coefficient can be modeled. The return signals after range compression and unfocused SAR processing, can be modeled as

$$\begin{aligned} v^{(1)}(r_0) &= A \int dS \chi_r(r_0 - r) \chi_{\phi}(\phi) \\ &\quad G^2(r, \phi) s(r, \phi) e^{2ikr} + n_1 \end{aligned} \quad (15)$$

$$\begin{aligned} v^{(2)}(r_0 + \Delta) &= A \int dS \chi_r(r_0 + \Delta - r') \chi_{\phi}(\phi) \\ &\quad G^2(r', \phi) s(r', \phi) e^{2ikr'} + n_2 \end{aligned} \quad (16)$$

where A is a constant which depends weakly on range; Δ is a delay introduced to coregister the two channels; χ_r is the system range point target response; χ_{ϕ} is the unfocused SAR azimuth response which is assumed to be a function of azimuth angle only since typically the range resolution is such that the change in Doppler with range can be ignored over one range resolution cell; $G^2(r', \phi)$ is the system antenna pattern; r and r' represent the range from the reference and secondary antennas to the surface; n_1 and n_2 represent the thermal noise in channels 1 and 2, respectively, and are assumed to be uncorrelated white noise processes with variance N ; and, finally, $s(r', \phi)$ represents

the surface rough surface brightness which is assumed to satisfy

$$\langle s(\mathbf{r})s^*(\mathbf{r}') \rangle = \delta(\mathbf{r} - \mathbf{r}')\sigma_0 \quad (17)$$

where σ_0 is the normalized radar cross section. Equation (17) is consistent with the deep phase approximation in rough surface scattering [20], which applies when the surface rms roughness is large compared to the wavelength. That approximation is valid for all the systems studied. Notice that we assume that the radar cross section is constant over the radar resolution cell, and the effect of surface waves can be neglected. The second assumption can be easily relaxed, following [15], but makes little difference since typically the range resolution is much greater than the wave height, and dominates the decorrelation effect.

In the following derivation, we assume that the width of the antenna pattern in both range and azimuth is much greater than the range and azimuth system responses, so that the antenna gain can be taken outside the integral. (This assumption always holds true for the range direction, but may not be strictly true in the azimuth direction if the unfocused SAR integration time is small. In that case, we can replace the azimuth system response function by an effective response function which includes the azimuth variation of the antenna pattern, without any loss of generality). Furthermore, we can approximate

$$\begin{aligned} r - r' &\approx B [\sin(\theta - \alpha) - \sin \theta \cos \alpha (1 - \cos \phi)] \\ &\approx B \left[\sin(\theta - \alpha) - \sin \theta \cos \alpha \frac{\phi^2}{2} \right] \end{aligned} \quad (18)$$

where we have made use of the fact that the azimuth beamwidth of a typical system is much smaller than 1. Expanding about r_0 and $\theta_0 = \arccos(H/r_0)$, this can be further approximated as

$$\begin{aligned} r - r' &\approx B \left[\sin(\theta_0 - \alpha) - \sin \theta_0 \cos \alpha \frac{\phi^2}{2} \right. \\ &\quad \left. + B \cos(\theta_0 - \alpha) \cos \theta_0 \frac{\rho}{r_0} \right] \end{aligned} \quad (19)$$

where terms of order $(R/(\sin \theta_0 r_0))^2$, where R is the system range resolution, have been neglected.

Using the previous results, we obtain the following expression for the complex correlation coefficient

$$\frac{\langle v^{(1)}v^{(2)*} \rangle}{\sqrt{\langle v^{(1)}v^{(1)*} \rangle \langle v^{(2)}v^{(2)*} \rangle}} = e^{i\Phi} \gamma_G \gamma_\phi \gamma_N = e^{i\Phi} \gamma \quad (20)$$

where Φ is the interferometric phase, and the geometric (γ_G), angular (γ_ϕ), and noise (γ_N) correlation factors are given by

$$\gamma_N = \frac{1}{1 + \text{SNR}^{-1}} \quad (21)$$

$$\gamma_G = \frac{\int_{-\infty}^{+\infty} d\rho \exp[i\kappa_\rho \rho] \chi_r(\rho) \chi_r^*(\rho + \delta)}{\int d\rho \chi_r(\rho) \chi_r^*(\rho + \delta)} \quad (22)$$

$$\gamma_\phi = \frac{\int_{-\pi}^{+\pi} d\phi \exp\left[-ikB \sin \theta_0 \cos \alpha \frac{\phi^2}{2}\right] |\chi_\phi(\phi)|^2}{\int d\phi |\chi_\phi(\phi)|^2} \quad (23)$$

where δ is the residual misregistration error, SNR is the system signal-to-noise ratio, and

$$\kappa_\rho = \frac{kB_\perp}{r_0 \tan \theta_0}$$

is the interferometric fringe wavenumber projected onto the tangent plane.

The result obtained for the correlation function shares the geometric and noise correlation terms with the standard SAR interferometry [15], but has an additional angular correlation factor, which is peculiar to unfocused SAR or real aperture radar configurations. The noise decorrelation term, γ_N , is common to the cross-correlation of any two signals with additive uncorrelated white noise. The geometrical decorrelation term, γ_G can be thought as being due to the fact that the interferometric phase is not constant as the cross-track distance varies across the resolution cell, giving rise to washing out of the interferometric fringes. The angular correlation coefficient, γ_ϕ , is then due to the fact that, for low azimuth resolutions, the range curvature of the resolution cell induces additional fringe averaging, further decreasing the correlation. In the limit of infinite bandwidth, the geometric decorrelation goes to 1, but the angular decorrelation factor remains. Note that by suitably shaping the return spectrum for each channel [21], both correlation coefficients can be made equal to one, at the expense of additional processing and range resolution. Due to the limitations imposed by on-board processing, this technique is not assumed for our design.

4.3 Geophysical Errors

To accurately reconstruct the ocean height, we not only need to know the geometric parameters discussed in section 4.1 above; we must also know the range r_0 to use in (1), (2) and (4). The range is accurately measured by timing aboard the spacecraft, and thus any additional delays caused by propagation of systematic biases produced by surface scattering effects must be compensated. For nadir-looking altimetry, these effects are well-known: ionospheric delay, dry and wet tropospheric delay, and Electromagnetic Bias.

The ionosphere index of refraction is non-unity and also dispersive, causing a frequency-dependent delay and corresponding range error in the radar signal [22]

$$\Delta r_I = 40.3 \frac{N_t}{f^2}$$

where Δr_I is the ionospheric range error (m), N_t is the columnar electron density ($1/m^2$), and f is frequency in Hz. N_t generally ranges from $20 \times 10^{16} - 100 \times 10^{16}$ electrons/ m^2 , producing range errors of 22–112 cm for C-band and 6–22 cm for Ku-band [22]. Scale sizes for ionospheric structures are generally quite large, of the order approximately 500 km or larger, so the error does not change rapidly with position, but its value is sufficiently large that it must be removed. The TOPEX altimeter uses simultaneous measurements at both Ku and C and the dispersion relation to solve for the delays at both wavelengths. Since the scale sizes are so large, similar measurements by a nadir-looking altimeter are sufficient to correct for this error in the interferometric SAR altimeter case as well.

Passage of the radar signal through the lower atmosphere also produces substantial delays, which can be estimated for the nadir-looking case by a combination of models and measurements. The index of refraction of the troposphere can be expressed as

$$n_{TROPO} = 1 + \delta_d + \delta_w$$

where δ_d is the dry troposphere component and δ_w the wet troposphere component, caused by the presence of water, liquid and vapor, in the ray path. The dry troposphere height correction for T/P is a modified Saastamoininen model [23]

$$\Delta r_d = -2.277 \times 10^{-3} (1 + 0.0026 \cos(2\phi)) P_s$$

where Δr_d is the dry tropo range error in m, ϕ is the latitude, and P_s is surface pressure in mBar. The correction for normal atmospheric pressure is 2.3m, and the scale size is basically the scale size of surface pressure variations. The wet tropospheric correction, by contrast, is smaller, but less stable, as it can have components with significant variability on the order of cloud sizes (1–5km). The wet tropo error is a function of integrated water vapor density, temperature, and integrated cloud moisture, and is typically 3–30 cm. The T/P instrument measures the water content and temperature using an inversion of three radiometer measurements at 18, 21, and 37 GHz to estimate the wet tropospheric delay.

Finally, the height distribution of the ocean surface caused by ocean waves introduces a bias in the height estimate compared to the true mean height. This is due to the fact that the wave

troughs tend to be brighter and thus weighted more heavily in the altimeter estimates than the wave peaks. This error is the EM bias [24] and can to first order be estimated as

$$\Delta r_{EM} = (0.013 + 0.0026U)SWH$$

where SWH is the significant wave height of the ocean surface measured by the altimeter waveform and U is the surface wind velocity estimated by the altimeter σ_0 . The EM bias error can also be estimated by more elaborate methods using more parameters or non-parametric forms [25] [26].

The effects of the medium on an interferometric SAR such as the instrument considered here are similar to its effects on a nadir-looking altimeter, and the corrections the same, to first order in the excess refractive index, δ , if we assume refractive index of the form $n = 1 + \delta$, where δ is a function of height. It can be shown [27] that the difference between the geometrical range r and the electromagnetic path length \tilde{r} may be expressed as

$$\begin{aligned}\tilde{r} &= r \left[1 + f_{(1)} - \frac{1}{2} \left[\left(\frac{r}{h} \right)^2 - 1 \right] (f_{(2)} - f_{(1)}^2) \right] \\ &= r + \delta r_n + \delta r_p\end{aligned}\tag{24}$$

where h is the height of the platform and $f_{(n)}$ are the moments of δ

$$f_{(n)} = \frac{1}{h} \int_0^h \delta^n(z) dz .$$

The first order correction δr_n depends only on the refractive index corrections and is just the sum of the range corrections as in the nadir-looking altimeter case. The second-order correction δr_p corresponds to the increase in path length due to ray bending and is proportional to the variance of the excess refractive index along the path. This term is in general much smaller than the first order term, e.g. the dry atmosphere ray bending error correction is 0.34 mm, much less than the 2.3 m from the first order term. The other media errors behave similarly, so for this instrument geometry, we can neglect the ray bending term and need only consider the refractive index corrections.

5 Calibration for Systematic Error Removal

In the previous section we see that direct measurement of the roll angle of the interferometric baseline is beyond the state of current technology. In this section, we propose two techniques for removing roll errors using the instrument data itself. The first technique uses the fact that the nadir altimeter is nearly insensitive to roll errors, so that a direct comparison of interferometer and altimeter data allows for the continuous estimation of the baseline roll. The second technique

exploits the fact that, at cross-over points, a direct comparison can be made between the nadir altimeter and the interferometer. Furthermore, at cross-over points the interferometer errors are separable, and can be estimated from the cross-over differences themselves.

A critical factor in the success of either technique is the fact that the ocean signature and its variability can be neglected during the estimation. In the next two subsections, we justify this claim and derive bounds on the accuracy of the systematic error removal. We show that either of these techniques by itself is sufficient for removing roll errors at the centimetric level, and leave the optimal error estimation algorithm combining both algorithms for future study.

5.1 Along-Track Calibration

Our first method for estimating the effective roll errors makes use of the concurrent altimeter measurement, and assumes that the inner pixel of the interferometer should be the same height. We model the height measured by the altimeter at a point \mathbf{r} as

$$h_A(\mathbf{r}) = h_0(\mathbf{r}) + n_A \quad (25)$$

where $h_0(\mathbf{r})$ is the true height, and n_A is the altimeter noise. Similarly, the height measured by the interferometer is

$$h_I(\mathbf{r}') = h_0(\mathbf{r}') + n_I + \delta h_{\text{eff}} \quad (26)$$

where $h_0(\mathbf{r}')$ is the true height at a point \mathbf{r}' , n_I is the interferometer noise, and δh_{eff} is the effective roll error, induced by roll and phase errors as discussed in Section IV above. From (25) and (26) we estimate the effective height error as

$$\begin{aligned} \delta \hat{h}_{\text{eff}} &= h_I(\mathbf{r}') - h_A(\mathbf{r}) \\ &= h_0(\mathbf{r}') + n_I + \delta h_{\text{eff}} - h_0(\mathbf{r}) - n_A \\ &= \delta h_{\text{eff}} + \Delta h(\mathbf{r}' - \mathbf{r}) + N \end{aligned} \quad (27)$$

where $N = n_I - n_A$ and $\Delta h(\mathbf{r}' - \mathbf{r}) = h_0(\mathbf{r}') - h_0(\mathbf{r})$. As we would expect, the error in estimating the tilt is due to the differences in the true heights at \mathbf{r}' and \mathbf{r} , and the measurement noise.

The quantity $\Delta h(\mathbf{r}' - \mathbf{r})$ depends on the geoid (Δh_g) and sea-surface (Δh_h) height changes on spatial scales of $\mathbf{r}' - \mathbf{r}$. We can model the sea-surface portion as

$$\langle \Delta h_h^2(\mathbf{r}' - \mathbf{r}) \rangle = \sigma_h^2(1 - C(|\mathbf{r}' - \mathbf{r}|)) \quad (28)$$

where σ_h^2 and $C(|\mathbf{r}' - \mathbf{r}|)$ are the spatial variance and autocorrelation function for the sea-surface height, respectively. Following Stammer [9], we have used TOPEX along-track data to estimate

those quantities. For 100 km of along-track averaging, we find the global $\sigma_h^2 \approx 60 \text{ cm}^2$. Given that result and the measured correlation function, we calculate the error at our first pixel (centered at $x_0 = 22 \text{ km}$) and propagate the roll error across the swath by x_i/x_0 , as suggested by (8). The results of that process are shown in the first row of Table 2. The swath position is measured from the center of each of the 6 pixels, assuming a 2.4° look angle, a 3.4° beamwidth, and a resolution of 14 km, all of which are discussed in Section VI below.

The second row of Table 2 contains the total height error due to errors in estimating the effective roll. It includes the root-sum squared tally of Δh_h , as well as pessimistic estimates of the relative geoid error (1 cm at the first pixel and propagated across the swath) and the altimeter and interferometer noise (1.7 cm after 100 km of averaging; see section VI below). The majority of the instrument swath is within an acceptable error range, although the errors in the outer two pixels are somewhat high.

Surprisingly, we cannot improve the error in the outer swath by moving the location of the first pixel to be closer to the nadir altimeter track. Using (28) and assuming a fixed swath width of $x = x_0 + x_i$, we can write the error at the outer swath as a function of x_0 :

$$\Delta h_h(x_0) = \frac{\sigma_h (x_0 + x_i)}{x_0} (1 - C(x_0))^{1/2} . \quad (29)$$

Using our measured sea-surface height correlation function for $C(x_0)$, we find that this function reaches a minimum near 22 km; at closer distances, the $(1 - C(x_0))$ term falls off slower than the $1/x_0$ term, yielding a larger error. Thus the only way to improve the along-track calibration is to average for longer periods, increasing the risk of having appreciable spacecraft roll during the averaging time. A second possibility for improving the outer swath error is to use the co-located data from the altimeter/interferometer cross-overs, and that method is discussed in the next section.

5.2 Calibration Using Cross-Overs

At each cross-over point, we model the ascending (A) or descending (D) interferometer height measurements, $h_I^{(A/D)}$, as

$$\begin{aligned} h_I^{A/D}(\mathbf{r}, t_{A/D}) &= h_O(\mathbf{r}, t_{A/D}) + C_{A/D} \delta \alpha_{A/D} \\ &\quad + C_{A/D} S_{A/D} \delta \dot{\alpha}_{A/D} \\ &\quad + n_I^{A/D}(C_{A/D}) \end{aligned} \quad (30)$$

where $S_{(A/D)}$ and $C_{(A/D)}$ are coordinates in the along and across-track directions, respectively; $h_O(\mathbf{r}, t_{A/D})$ is the true sea surface height measured at location \mathbf{r} and time $t_{A/D}$; and $n_I^{A/D}(C_{A/D})$

represents the interferometer measurement noise, which is a function of the cross-track coordinate alone (see (8)), and is independent between resolution cells.

In modeling the systematic error, it is assumed that in the interval between cross-over points the roll error can be assumed to vary linearly:

$$\delta\alpha(S_{A/D}) = \delta\alpha(0) + \delta\dot{\alpha}S_{A/D} . \quad (31)$$

Under most space-borne circumstances, this is a reasonable assumption given the slowly varying environment in space on time-scales on the order of one minute, and the short times spent in cross-over diamond, which are on the order of half a minute. The linear assumption is also probably sufficient for interpolation between different calibration regions, given the time between interferometric diamonds or cross-over points, as shown in Fig. 8.

The nadir altimeter measurement, $h_A^{A/D}(\mathbf{r}, t_{A/D})$, resampled to the same resolution as the interferometric measurement grid, is modeled as

$$h_A^{A/D}(\mathbf{r}, t_{A/D}) = h_O(\mathbf{r}, t_{A/D}) + n_A^{A/D} \quad (32)$$

where $n_A^{A/D}$ is the altimeter height measurement noise, which we take to be spatially constant and independent between resolution cells.

The height differences at the overlap regions between ascending and descending passes can then be written as

$$\delta h_{IA} = h_I^{A/D}(\mathbf{r}, t_{A/D}) - h_A^{D/A}(\mathbf{r}, t_{D/A}) \quad (33)$$

$$= C_{A/D}\delta\alpha_{A/D} + C_{A/D}S_{A/D}\delta\dot{\alpha}_{A/D} + N_{IA} \quad (34)$$

for interferometer-altimeter overlaps, and

$$\delta h_{II} = h_I^A(\mathbf{r}, t_A) - h_I^D(\mathbf{r}, t_D) \quad (35)$$

$$= C_A\delta\alpha_A + C_AS_A\delta\dot{\alpha}_A - C_D\delta\alpha_D - C_DS_D\delta\dot{\alpha}_D + N_{II} \quad (36)$$

for the interferometer-interferometer overlaps. These equations can be inverted, by using maximum likelihood estimation, to estimate the roll error parameters, $\delta\alpha_{A/D}$ and $\delta\dot{\alpha}_{A/D}$. The “noise” terms, N_{IA} and N_{II} , have contributions due to the random measurement noise and to changes in the sea surface height between passes:

$$N_{IA} = h_O(\mathbf{r}, t_{A/D}) - h_O(\mathbf{r}, t_{D/A}) + n_I^{A/D} - n_A^{D/A} \quad (37)$$

$$N_{II} = h_O(\mathbf{r}, t_A) - h_O(\mathbf{r}, t_D) + n_I^A - n_I^D . \quad (38)$$

To estimate the optimal weights for fitting the roll error parameters, it is required that the statistics for the error be known. The instrument measurement errors are assumed to be zero-mean Gaussian random variables, uncorrelated from point to point, and between instruments. Their standard deviations are given by σ_A and $\sigma_I(C_{A/D})$, for the altimeter and interferometer respectively.

The ocean surface variability is spatially and seasonally varying, but we assume that, over the short time and spatial scales used for the cross-over calibration, it can also be treated as a homogeneous correlated Gaussian random process whose statistical characteristics are determined by a spatially varying height standard deviation, σ_0 , and a space-time correlation function, $C(|\mathbf{r} - \mathbf{r}'|, |t - t'|)$. Under these assumptions, the statistical characteristics of the ocean variability contribution to the cross-over measurement noise is given by

$$\begin{aligned} & \langle (h_O(\mathbf{r}, t_A) - h_O(\mathbf{r}, t_D))(h_O(\mathbf{r}', t_A) - h_O(\mathbf{r}', t_D)) \rangle \\ &= 2\sigma_O^2(\mathbf{r})([C(|\mathbf{r} - \mathbf{r}'|, 0) - C(|\mathbf{r} - \mathbf{r}'|, |t_A - t_D|)]) . \end{aligned} \quad (39)$$

To assess the cross-over calibration accuracy, we use a 1/6 degree resolution eddy-resolving ocean circulation model of the Atlantic provided by Y. Chao [16]. The model ranges from latitudes of 0° and 22° and longitudes of -89° and -42° , and is chosen for two reasons: first, as can be seen in Fig. 9, it includes a street of strong mesoscale variability due to continuous presence of eddies which follow the coast of South America and end up in the Gulf of Mexico. Second, the revisit time between cross-over points is at its largest close to the equator, and coverage is minimized, so that only information from two tracks can usually be used for the inversion.

The accuracy of the estimated parameters depends on the number of cross-overs which can be used simultaneously in the estimation. In order to obtain the most conservative estimate, we assume that there is no overlap between cross-over regions so that each set of fitting parameters is estimated independently. In practice, as one sees from Fig. 8, the amount of overlap can be substantial, so that our current estimate underestimates the accuracy with which the calibration parameters can be inverted. We use the system parameters given in Section 6 but, again conservatively, assume that the interferometric measurement error has a constant standard deviation of 6 cm across the swath. The nadir altimeter system standard deviation is assumed to be 2 cm. The ocean correlation function is assumed to be Gaussian, with a correlation time of 11 days, obtained from the entire simulated data set. The simulation is run over the entire area shown in Fig. 9 for a period of 270 days.

At each cross-over point, 1000 independent realizations of the interferometric measurement are generated, and the calibration parameters are estimated using the procedure outlined above. Histograms of the results for the estimated roll and roll rate errors are presented in Figs. 10 and 11.

It is evident from these figures that the baseline roll can be measured consistently better than the roll accuracy goal of 0.1 arcsec mentioned earlier. Similarly, the roll-rate accuracy is also measured substantially better than 0.01 arcsec/sec. Figs. 12 and 13 show the implications of these results for the height errors. As can be seen, the roll errors over most of the swath are small compared to the mesoscale eddy signatures, and even at the far swath, the systematic errors are less than 4 cm for the worst case. These results indicate that the cross-over technique is sufficient to remove systematic roll errors which conform to the linear change assumption used in the simulation. The effect of random variations superimposed on this linear trend are currently under investigation. The ultimate accuracy of this technique can be improved when multiple cross-overs are used in the estimation, and this study is also underway. However, even given the pessimistic assumptions in the current simulation, we conclude that the cross-over technique is sufficient for the satisfactory removal of small systematic errors at a level sufficient for the investigation of mesoscale oceanography.

6 Sample System Performance

In this section, we present the design and performance of a sample wide-swath interferometer system. The next subsection details the instrument characteristics, while the following subsections discuss the random, media propagation, and total height error performance for the sample system, respectively.

6.1 Instrument Characteristics

Table 3 shows the key system parameters for a sample wide-swath interferometric system. As stated above, we have assumed a orbit similar to T/P, 1336 km, to achieve the desired temporal sampling and reduce tidal aliasing. We have also chosen a frequency similar to that of T/P, 13.6 GHz, to facilitate the use of a Ku-band altimeter media correction on the interferometer.

The system swath is designed to extend from 15 km to 100 km on either side of the nadir track, and the nominal pixel size is 14 km by 14 km. Those requirements, along with the desire to maintain a reasonable signal-to-noise ratio, determine the antenna dimensions shown. A very short, 5-pulse, synthetic aperture is formed, and we use a large number of incoherent averages to reduce the random height noise of the instrument (900 in the along track direction, and from 28 to 118 in the range direction).

In order to estimate the system's SNR for typical ocean conditions, we use the altimeter wind speed model function of Freilich and Challenor [28], and, following their results, approximate the global wind speed distribution by a Rayleigh distribution with a mean 19.4 m wind speed of 7.4 m/s. The off-nadir backscatter cross section is assumed to be given by the specular-point geometrical

optics result for the backscatter cross section [20]

$$\sigma_0(\theta) = \frac{|R|^2}{s^2 \cos^4 \theta} \exp \left[-\frac{\tan^2 \theta}{s^2} \right] \quad (40)$$

where $|R|^2 \approx 0.61$ is the ocean reflection coefficient, and s^2 is the effective surface slope variance for Ku-band. We use the Freilich and Challenor nadir incidence model function and (40) in order to estimate the effective slope variance as a function of wind speed. Using the Rayleigh distribution assumption and the radar equation with the system parameters given in Table 3 together with (40), we can calculate the predicted system SNR for any desired percentile of global wind speed conditions. Fig. 14 presents the predicted system SNR as a function of cross-track distance for the median (7m/s wind speed, $\sigma_0 = 10.8$ dB, $s = 12.7^\circ$) and 90-percentile (14.5 m/s wind speed, $\sigma_0 = 9$ dB, $s = 15.6^\circ$) conditions.

The results in this figure indicate that the system performance is not very sensitive to wind speed variations, reflecting the weak dependence of the radar cross section on wind speed. Near the edges of the swath, the 95-percentile SNR can be as low as 7 dB, given the 120 W transmit power. To increase the SNR appreciably while maintaining our current power budget, we would have to increase the size of the antenna substantially. In order to keep the swath width constant, however, we can only change the azimuth dimension of the antenna, which is already somewhat large at 2.5 m. An even larger antenna becomes significantly more difficult to deploy, and adds to the mass and cost of the system design. Nevertheless, as we see below, an adequate height noise value is achieved due to the large number of looks taken.

6.2 Random Error Budget

Given the system with parameters of Table 3, we can estimate the random component of the height error using the model of Section 4.2.

The correlation factors for thermal noise (γ_N), geometry (γ_G), and angular or range curvature (γ_ϕ) may be computed from (21), (22), and (23) using the SNR and geometry of the system, and assuming sinc functions for the range and azimuth point target responses. The sinc function also allows separation of a misregistration correlation factor. The values of each of these factors is shown as a function of cross-track position, along with the total γ , in Fig. 15. Clearly, the total decorrelation is dominated by the thermal noise contribution and, in the near swath, by the geometric contribution.

Fig. 16 shows the median and 95-percentile height noise Δh obtained by substitution of the decorrelation γ into (13) and the result into (10). This random noise is less than about 3.5 cm in the first 5 pixels of the swath, but rises to about 4.7 cm for the final 14 km range bin in the swath.

Notice that this random noise estimate assumes only one look at a given area. However, during any given 10-day repeat cycle, every point is imaged at least twice, and as many as four times. Averaging of these estimates reduces the random noise component by a factor ranging from $1/\sqrt{2}$ to 2.

6.3 Geophysical Delays Error Budget

As discussed in Section IV C, altimeters must correct for the delays from the ionosphere, delays from the wet and dry troposphere, and the effects of the Electromagnetic Bias. In order to achieve centimetric accuracy with the interferometer, we must also correct its height estimates accordingly. Ideally, we would like to use the altimeter corrections for the interferometer, removing the need for an off-nadir-looking radiometer and dual frequency radar system. In this section we test the feasibility of that method by examining the distance dependence of TOPEX media corrections from TOPEX data.

We have chosen four TOPEX cycles spaced evenly throughout the year, and examined the rms height correction differences as a function of distance along the altimeter track. Fig. 17 shows the rss media error correction differences from the four media corrections as a function of distance. The solid line is the global mean value, while the dashed lines represent the minimum and maximum values when the data is grouped into 10° latitude bands from -65° to 65° latitude. The maximum occurs, as would be expected, in the band that straddles the equator.

From Fig. 17, we see that error in correcting the outer interferometer pixel with the altimeter media corrections is less than 1.8 cm in the mean case, and approximately 2.2 cm in the worst case. The mean differences are even smaller over much of the swath. Those values suggest that the height accuracy of the interferometer should not be severely effected by the use of the nadir-looking media corrections, significantly simplifying the overall system complexity, as well as reducing the mass, power, and volume requirements.

An improvement over the errors implied by Fig. 17 could perhaps be best accomplished by the addition of an off-nadir looking radiometer, correcting for the wet troposphere delays in the outer swath. Table 4 shows the proportion of the total, rss error from the four media sources at the inner and outer pixels of the swath. As expected, the wet troposphere difference dominates in the outer swath due to its shorter correlation length, while the ionosphere, with its long correlation length, remains roughly constant.

6.4 Total Error Budget

In the above sections we have discussed the residual attitude and phase errors, the random error budget, and the errors due to the use of the nadir media corrections. We can now determine the total interferometric height budget, based on our sample system design.

Table 5 summarizes the errors discussed in the previous sections, and shows the total rss height error budget. The media errors and EM bias errors are likely pessimistic, and the additional cross-track propagation errors are included in the row of media correction errors (Section 6.3). The residual attitude errors are taken from the cross-over calibration (Section 5.2), and may be improved by an optimal combination of along-track and cross-over calibration techniques. The dominant error source is, as discussed, the height noise, and could be reduced by increased SNR, additional spatial averaging, or a longer baseline. Even for the pessimistic estimate presented here, the average height noise over the swath is only about 3 cm and the average systematic noise is also about 3 cm, which are sufficient for the mesoscale mapping applications for which this concept is designed.

7 Conclusions

This paper presents a new system concept for ocean altimetry designed to provide coverage for a portion of the ocean variability spectrum that is not currently available: the mesoscale eddy field. The instrument consists of a wide-swath (200km) interferometric radar combined with a nadir-looking 2-frequency altimeter and radiometer. This concept allows a single-platform instrument to produce near global coverage of the ocean surface and direct measurement of 2D geostrophic velocity with temporal resolution similar to TOPEX/Poseidon.

We have discussed the measurement concept, error models, and the self-calibration scheme using the nadir altimeter data and ascending/descending crossover data to remove residual attitude errors. Finally, we have presented a sample point design with average random errors of approximately 3 cm and resolution of 14 km. The residual systematic error of this design after calibration averages about 3 cm over the swath. The ocean mesoscale eddy field has height amplitudes of ~ 25 cm and spatial scales of 50–150 km, so such eddies should be clearly visible in the data product from this instrument. In fact, with eddy time scales of 30 days and a repeat time of 10 days for this design, and random errors only $\sim 12\%$ of the signal, accurate eddy identification and tracking should be possible, allowing more detailed study of energy flows in this region of the ocean variability spectrum than ever before.

Finally, we note that the concept presented here is not limited to oceanographic applications, but can be used whenever low spatial resolution and high vertical accuracy are desired. A prime

example of an alternate application would be the high precision mapping of the Antarctic or Greenland ice sheets. In this case, systematic and random errors could be greatly reduced due to the large degree of overlaps of a polar orbit, as well as the much longer temporal scales for surface change.

Acknowledgments

This work was conducted by the Jet Propulsion Laboratory, California Institute of Technology, under contract with the National Aeronautics and Space Administration (NASA). The authors would like to thank Dr. Yi Chao for providing the ocean simulation data, and Dr. Lee-Lueng Fu for helpful comments.

References

- [1] H.F. Deidel and B.S. Giese, "Equatorial currents in the Pacific ocean 1992-1997," *J. Geophys. Res.*, vol. 104, pp. 7849-7863, 1999.
- [2] D. B. Chelton and M. G. Schlax, "Global observations of oceanic Rossby waves," *Science*, vol. 272, no. 5259, pp. 234-238, 1996.
- [3] D. J. M. Greenslade, D. B. Chelton, and M. G. Schlax, "The midlatitude resolution capability of sea level fields constructed from single and multiple satellite altimeter datasets," *J. Atmos. Oceanic Technol.*, vol. 14, no. 4, pp. 849-870, 1997.
- [4] G. A. Jacobs and J. L. Mitchell, "Combining multiple altimeter missions," *J. Geophys. Res.*, vol. 102, no. C10, pp. 23187-23206, 1997.
- [5] G. B. Bush, E. B. Dobson, R. Matyskiela, C. C. Kilgus, and E. J. Walsh, "An analysis of a satellite multibeam altimeter," *Mar. Geod.*, vol. 8, no. 1-4, pp. 345-384, 1984.
- [6] M. Martin-Neira, C. Mavrocordatos, and E. Colzi, "Study of a constellation of bistatic radar altimeters for mesoscale ocean applications," *IEEE Trans. Geosci. Remote Sensing*, vol. 36, no. 6, pp. 1898-1904, 1998.
- [7] C. Koblinsky, P. Gaspar, and G. Lagerloef (eds.), "The future of spaceborne altimetry: oceans and climate change," Tech. Rep., Joint Oceanographic Institutions Inc., Washington D.C., 1992.
- [8] M.E. Parke, R.H. Stewart, D.L. Farless, and D.E Cartwright, "On the choice of orbits for an altimetric satellite to study ocean circulation and tides," *J. Geophys. Res.*, vol. 92, pp. 11693-11707, 1987.
- [9] D. Stammer, "Global characteristics of ocean variability estimated from regional TOPEX/Poseidon altimeter measurements," *J. Phys. Oceanogr.*, vol. 27, no. 8, pp. 1743-1769, 1997.
- [10] R. Morrow, R. Coleman, J. Church, and D. Chelton, "Surface eddy momentum flux and velocity variances in the southern-ocean from geosat altimetry," *J. Phys. Oceanogr.*, vol. 24, no. 10, pp. 2050-2071, 1994.
- [11] C. Wunsch and D. Stammer, "Satellite altimetry, the marine geoid, and the oceanic general circulation," *Annual Review of Earth and Planetary Sciences*, vol. 26, pp. 219-253, 1998.

- [12] G.A. Jacobs, C.N Barron, M.R. Carnes, D.N. Fox, Y.H. Hsu, H.E. Hurlburt, P. Pistek, R.C. Rhodes, W.J. Teague, J.P Blaha, R. Crout, E. Petruncio, O.M. Smedstad, and K.R. Whitmer, "Navy altimeter data requirements," *Stennis Space Center*, vol. MS 39529-5004, 1999.
- [13] C. Elachi, K. E. Im, F. Li, and E. Rodriguez, "Global digital topography mapping with a synthetic aperture scanning radar altimeter," *Int. J. Remote Sensing*, vol. 11, no. 4, pp. 585–601, 1990.
- [14] H.A. Zebker and R.M. Goldstein, "Topographic mapping from interferometric synthetic aperture radar observations," *J. Geophys. Res.*, , no. 91, pp. 4993–4999, 1986.
- [15] E. Rodriguez and J. M. Martin, "Theory and design of interferometric synthetic aperture radars," *IEEE Proceedings-F*, vol. 139, no. 2, pp. 147–159, 1992.
- [16] Y. Chao, A. Gangopadhyay, F. O. Bryan, and W. R. Holland, "Modeling the gulf stream system: How far from reality?," *Geophys. Res. Lett.*, vol. 23, no. 22, pp. 3155–3158, 1996.
- [17] J.A. Carton and Y. Chao, "Caribbean sea eddies inferred from TOPEX/Poseidon altimetry and a 1/6 degree atlantic ocean model simulation," *J. Geophys. Res.*, vol. 104, pp. 7743–7752, 1999.
- [18] A.J.E. Smith, E.T. Hesper, D.C. Kuijper, G.J. Mets, P.N.A.M Visser, B.A.C. Ambrosius, and K.F. Wakker, "TOPEX/Poseidon orbit error assessment," *J. of Geodesy*, vol. 70, no. 9, pp. 546–553, 1996.
- [19] E. Rodriguez, "Altimetry for non-gaussian oceans - height biases and estimation of parameters," *J. Geophys. Res.*, vol. 93, no. C11, pp. 14107–14120, 1988.
- [20] L. Tsang, J.A. Kong, and R.T. Shin, *Theory of Microwave Remote Sensing*, Wiley-Interscience, New York, 1985.
- [21] C. Prati, F. Rocca, A. Monti Guarnieri, and E. Damonti, "Seismic migration for SAR focusing: interferometric applications," *IEEE Trans. Geosci. Remote Sensing*, vol. 28, pp. 627–639, 1990.
- [22] J. Goldhirsh and J.R. Rowland, "A tutorial assessment of atmospheric height uncertainties for high-precision satellite altimeter missions to monitor ocean currents," *IEEE Trans. Geosci. Remote Sensing*, vol. GE-20, no. 4, pp. 418–434, 1982.
- [23] P. Callahan, "TOPEX ground system science algorithm specification," Tech. Rep. JPL D-7075, Jet Propulsion Laboratory, 1990.

- [24] E.J. Walsh, F.C. Jackson, E.A. Uliana, and R.N. Swift, "Observations on electromagnetic bias in radar altimeter sea-surface measurements," *J. Geophys. Res.*, vol. 94, no. C10, pp. 14575–14584, 1989.
- [25] E. Rodriguez and J.M. Martin, "Estimation of the electromagnetic bias from retracked TOPEX data," *J. Geophys. Res.*, vol. 99, no. C12, pp. 24971–24979, 1994.
- [26] P. Gaspar and J.P. Florens, "Estimation of the sea state bias in radar altimeter measurements of sea level: Results from a new nonparametric method," *J. Geophys. Res.*, vol. 103, no. C8, pp. 24619–24631, 1998.
- [27] E. Rodriguez, D.A. Imel, and S.N. Madsen, "The accuracy of airborne interferometric SAR's," Submitted to IEEE Trans. AES.
- [28] M.H. Freilich and P.G. Challenor, "A new approach for determining fully empirical altimeter wind speed model functions," *J. Geophys. Res.*, vol. 99, pp. 25051–25062, 1994.

List of Tables

1	Typical space-time signatures of ocean features	31
2	The difference in sea-surface height $\Delta h_h(\mathbf{r}' - \mathbf{r} = 22\text{km})$, for row 1, and the total rss error in the estimated tilt $\delta \hat{h}_{\text{eff}}$, for row 2.	32
3	Key system parameters for wide-swath interferometer system.	33
4	The components of the correction differences for the interferometer inner and outer pixels.	34
5	A breakdown of the total rss interferometric height error budgets. Included are the standard media corrections, the error induced across the swath by the use of the nadir media corrections, the residual attitude error after performing the cross-over attitude calibration, and the random height error components.	35

List of Figures

1	The space-time resolution capabilities for various single altimeter missions and proposed multi-altimeter configurations. The area above and to the right of any system design point measures the spatial and temporal resolution capabilities of that system of coordinated altimeter satellites. The shaded area represents the typical region of globally observed mesoscale eddies. Also included is the design point for the wide-swath altimeter system proposed in this paper. The track separation corresponds to the spacing of the wide swath pixels, and does not take into account the presence of the small gaps shown in Fig. 5.	36
2	Interferometric measurement geometry.	37
3	Proposed wide swath altimeter configuration using a nadir altimeter and two interferometric swaths to achieve a 200 km swath using the TOPEX/Poseidon orbit. . . .	38
4	Spatial coverage characteristics for the wide-swath and the TOPEX/Poseidon instruments, as a function of latitude. This data is generated by gridding the ocean into 0.05° by 0.05° bins, and by counting the percentage of bins that the TOPEX and wide-swath instruments would sample.	39
5	Low latitude spatial coverage map for the wide-swath instrument superimposed on eddies simulated using an eddy resolving circulation model for the Caribbean region. Notice that while data gaps exist, they are typically smaller than the eddy scales, due to the increase in the Rossby radius at lower latitudes.	40
6	Flow diagram for the interferometric onboard processing algorithm.	41
7	Geometry for cross-over calibration regions. Dashed areas represent interferometer-interferometer cross-overs. Thick solid lines represent altimeter-interferometer cross-overs.	42
8	Cumulative distribution function of the time between nadir altimeter cross-overs (dashed line), and the time between interferometric cross-over diamonds (solid line), for the TOPEX orbit, and assuming a 200 km interferometric swath. Note that due to the short distances between cross-overs at high latitudes, over half of the interferometric diamonds overlap.	43
9	Standard deviation of sea surface height over 270 days from the eddy-resolving circulation model used for the cross-over simulation. The corridor of eddy activity from South America to the Gulf of Mexico is clearly defined, with peak rms variability of about 30 cm.	44
10	Histogram of estimated roll errors for cross-over calibration simulation.	45

11	Histogram of estimated roll rate errors for cross-over calibration simulation.	46
12	Height errors induced by residual roll errors after cross-over calibration, as a function of cross-track distance. The three curves represent the minimum, mean and maximum errors in the simulation.	47
13	Height errors induced by residual roll rate errors after cross-over calibration, as a function of time from the cross-over point. The three curves represent the minimum, mean and maximum errors in the simulation.	48
14	Wide swath system predicted signal-to-noise ratio for median wind speed conditions (dashed line) and 95-percentile conditions (solid line).	49
15	Contributions to the interferometric correlation due to different sources of decorrelation, for 95-percentile conditions. The major source of decorrelation is thermal noise.	50
16	Predicted height noise as a function of the cross-track distance for a single pass interferometric measurement, assuming 14 km spatial resolution and median (dashed line) or 95-percentile (solid line) wind speed condtions. Height noise can be further reduced by averaging ascending and descending pass heights and by degrading the spatial resolution, if desired.	51
17	The total rss media correction value as a function of distance along the TOPEX track. The solid line is the globally averaged value, while the dashed lines are the minimum and maximum values when the data are grouped into bands of 10° in latitude. The maximum value occurs in the band straddling the equator.	52

Table 1:

Phenomena	Vertical Range (cm)	Spatial Scale (km)	Time Period (days)
Ocean Gyres			
Mean	100	> 1000	
Variations	10	> 1000	> 300
Mesoscale Eddies	25	~ 50	> 30
Western Boundary Currents			
Mean	100	100	
Variations	100	100	> 10
Eastern Boundary Currents			
Mean	20	500	
Variations	10	500	> 10
Equatorial Currents			
Mean	20	> 500	
Variations	10	> 500	> 50
El Niño Equatorial Response	20	> 500	~ 1000

Table 2:

Swath Position (km)	22	36	50	64	78	92
$\Delta h_h(\mathbf{r}' - \mathbf{r} = 22\text{km})$ (cm)	2.7	4.4	6.1	7.8	9.5	11.2
$\delta \hat{h}_{\text{eff}} - \delta h_{\text{eff}}$ (cm)	3.3	4.8	6.4	8.0	9.7	11.4

Table 3:

Parameter	Units	Value
frequency	GHz	13.6
bandwidth	MHz	15
pulse length	μsec	50
peak transmit power	Watts	120
system losses	dB	-3
baseline length	m	7
antenna efficiency	dB	-3
antenna width	m	0.3
antenna length	m	2.5
atmospheric loss	dB	-1
platform height	km	1336
near-swath look angle	deg	0.64
boresight look angle	deg	3.2
far-swath look angle	deg	4.3
swath	km	85
minimum cross track distance	km	15
no. coherently averaged pulses	-	5
no. incoherently averaged cells	-	900
prf	Hz	4000

Table 4:

Error Source	Wet Tropo	EM Bias	Ionosphere	Dry Tropo	RSS Total
Inner swath (22 km) [cm]	0.53	0.55	0.65	0.06	1.0
Outer swath (92 km) [cm]	1.39	0.80	0.72	0.17	1.8

Table 5:

Cross-Track Distance [km]	22	36	50	64	78	92
Ionospheric Error [cm]	1.0	1.0	1.0	1.0	1.0	1.0
Tropospheric Error [cm]	1.0	1.0	1.0	1.0	1.0	1.0
EM Bias [cm]	2.0	2.0	2.0	2.0	2.0	2.0
Media Correction Error [cm]	1.0	1.2	1.3	1.5	1.6	1.8
Residual Attitude [cm]	0.9	1.4	2.0	2.6	3.1	3.7
Median Height Noise [cm]	3.1	3.0	2.8	3.0	3.4	4.2
95% Height Noise [cm]	3.4	3.2	3.1	3.3	3.8	4.8
Median RSS Error [cm]	4.2	4.3	4.4	4.9	5.5	6.4
95% RSS Error [cm]	4.4	4.4	4.6	5.1	5.7	6.8

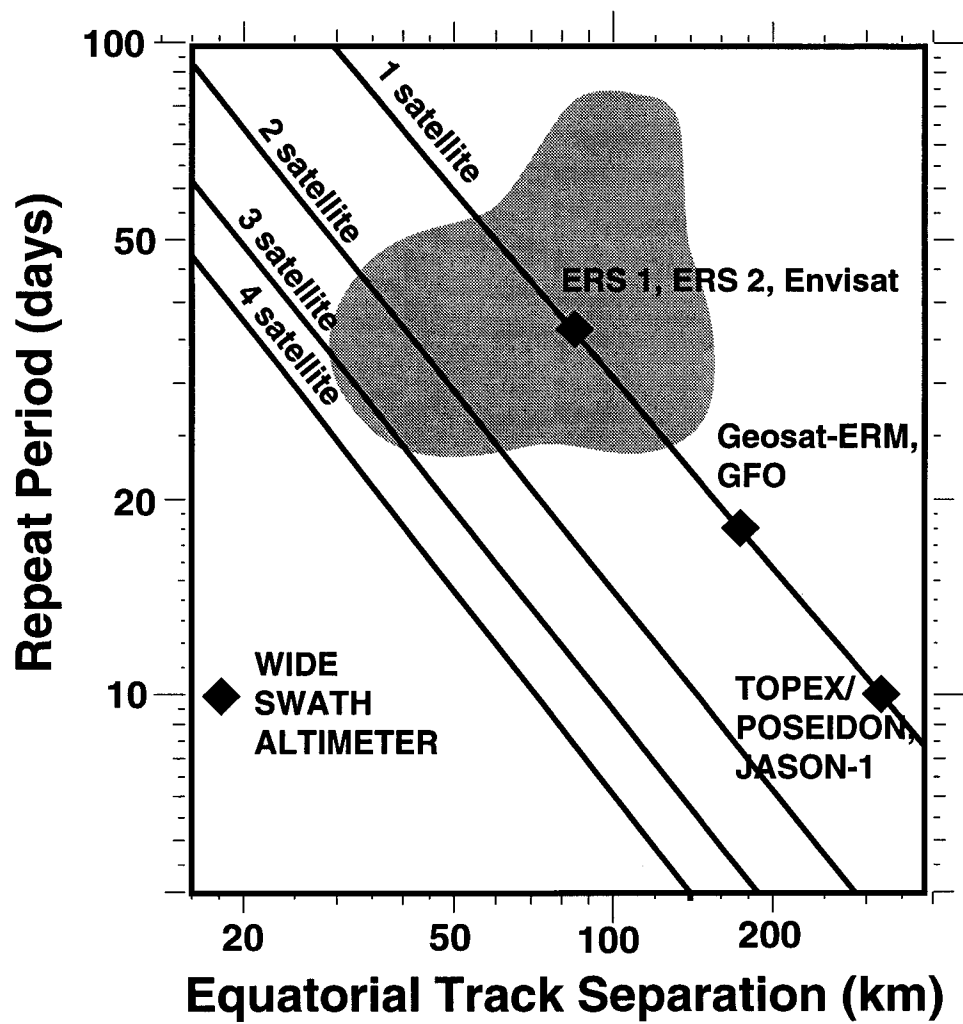


Figure 1:

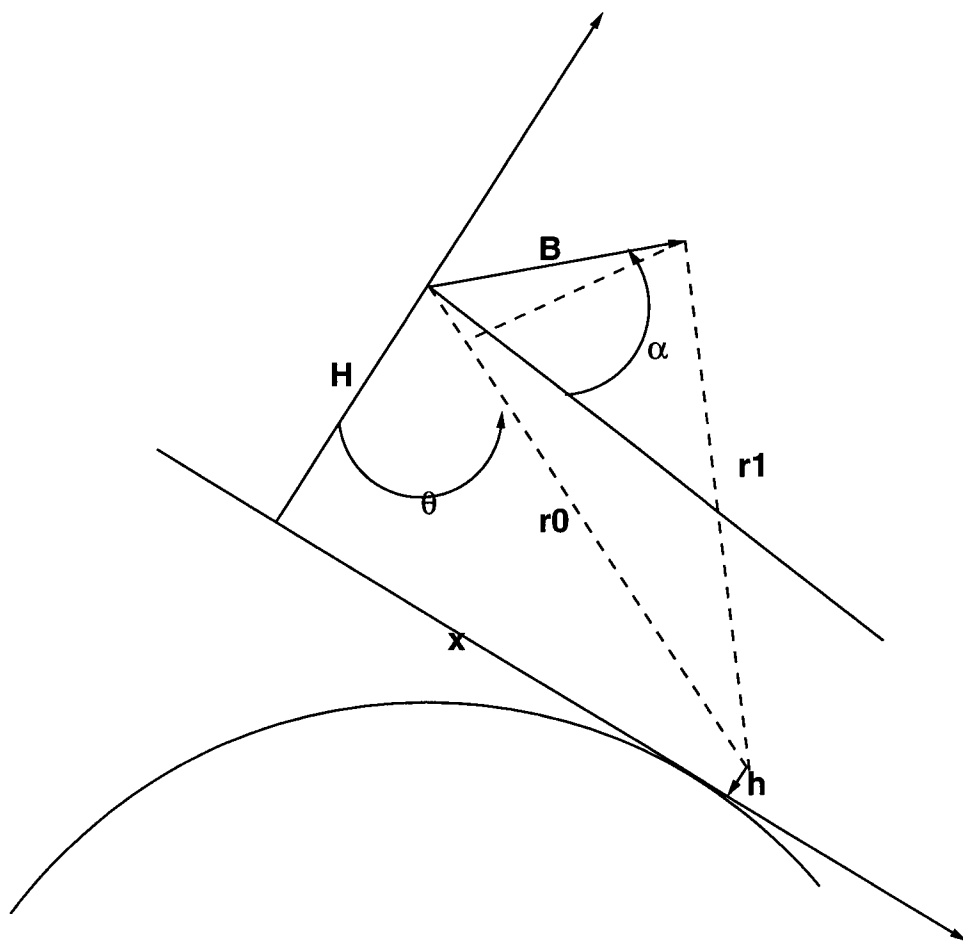


Figure 2:

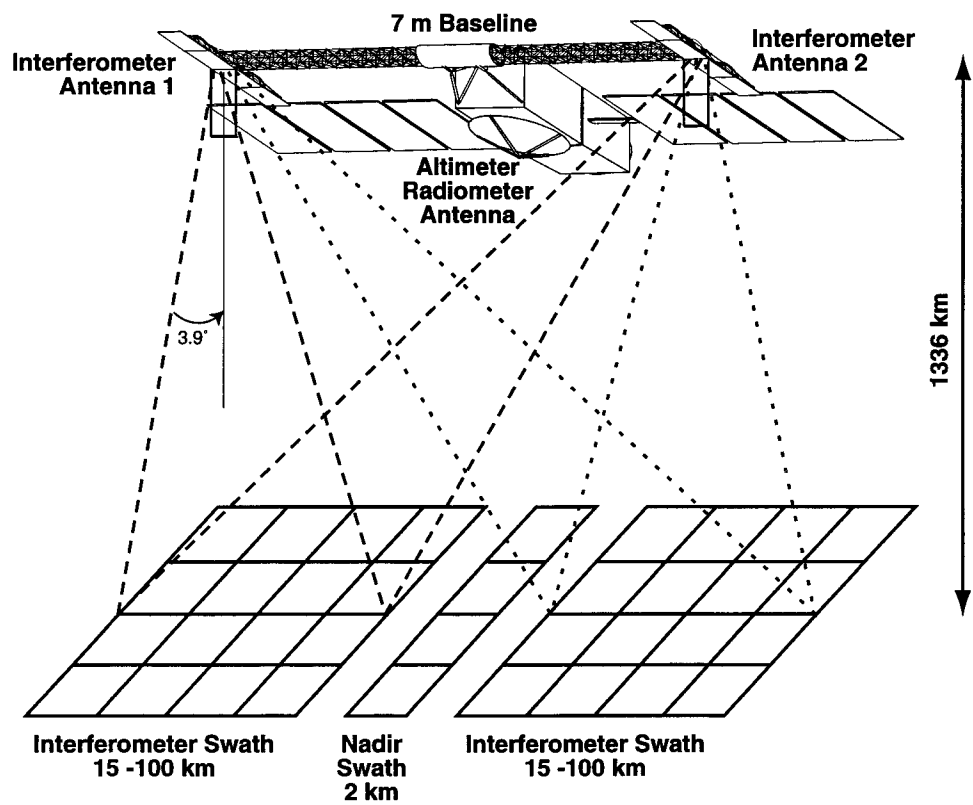


Figure 3:

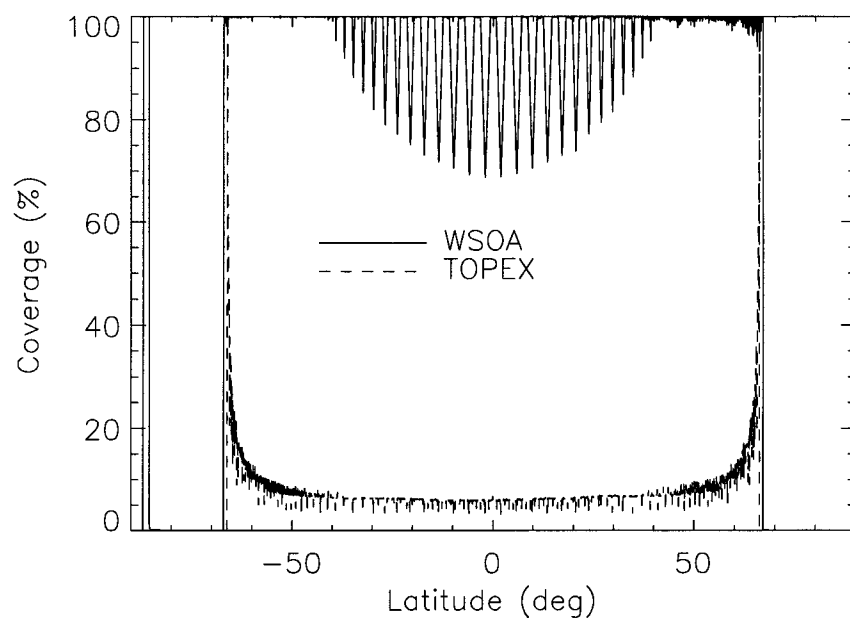


Figure 4:

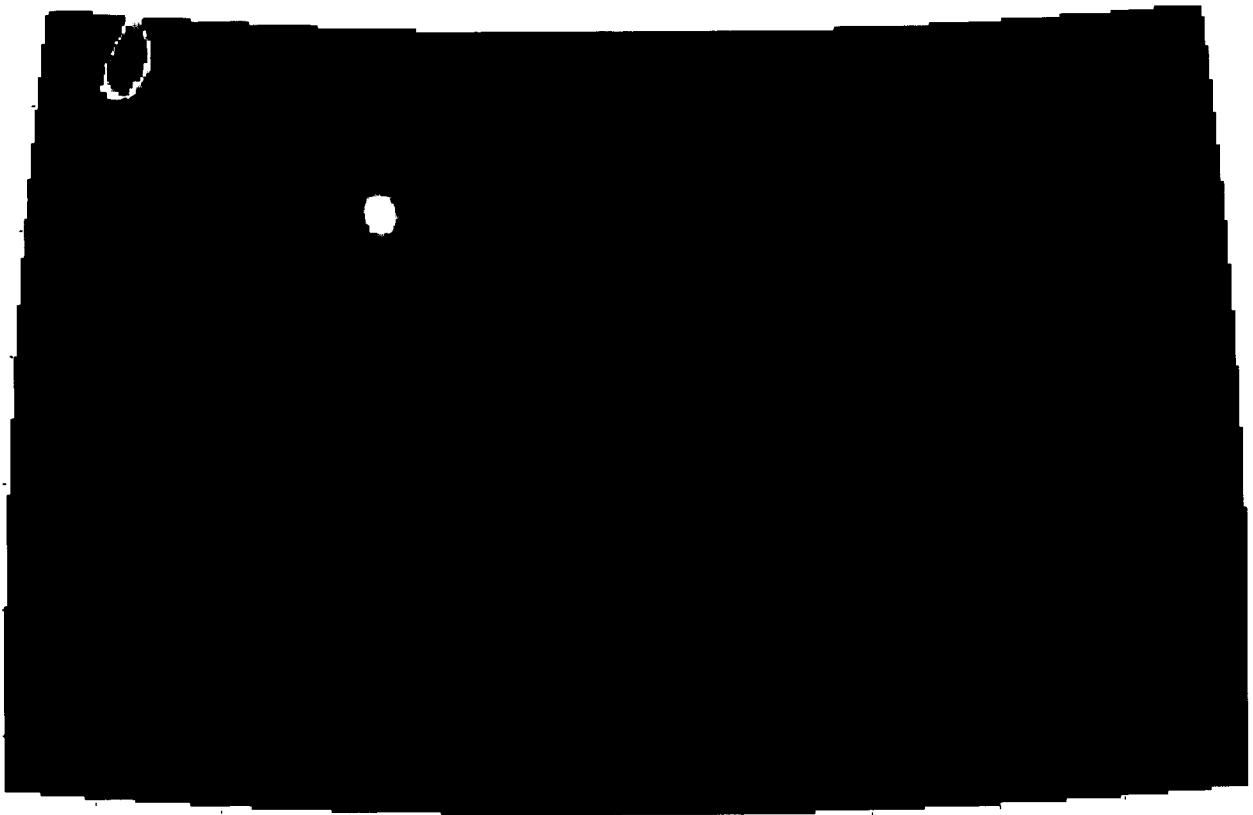


Figure 5:

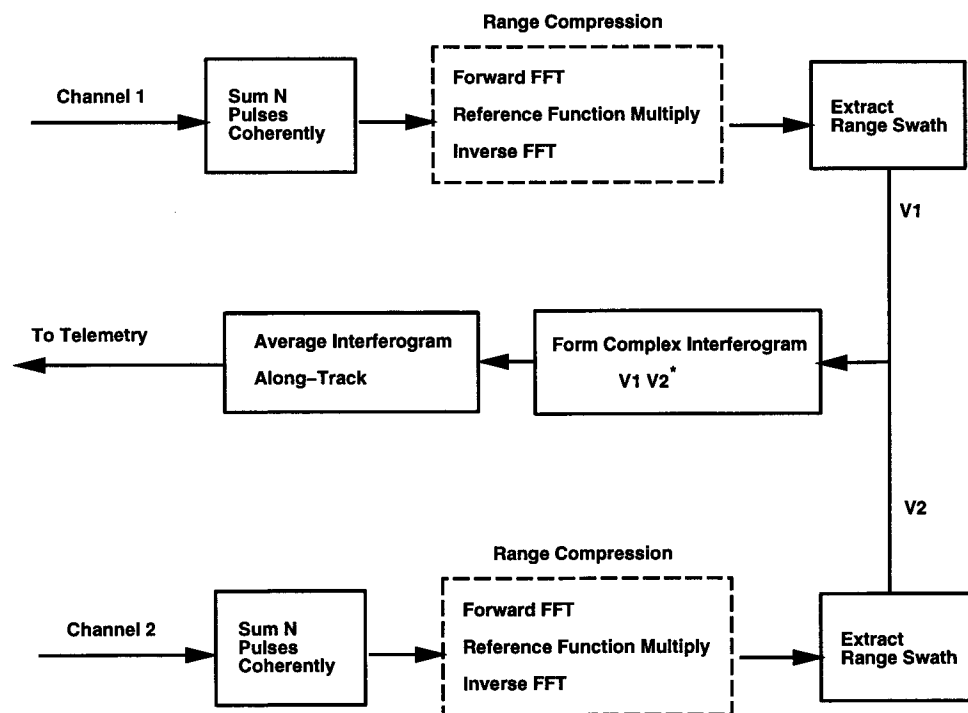


Figure 6:

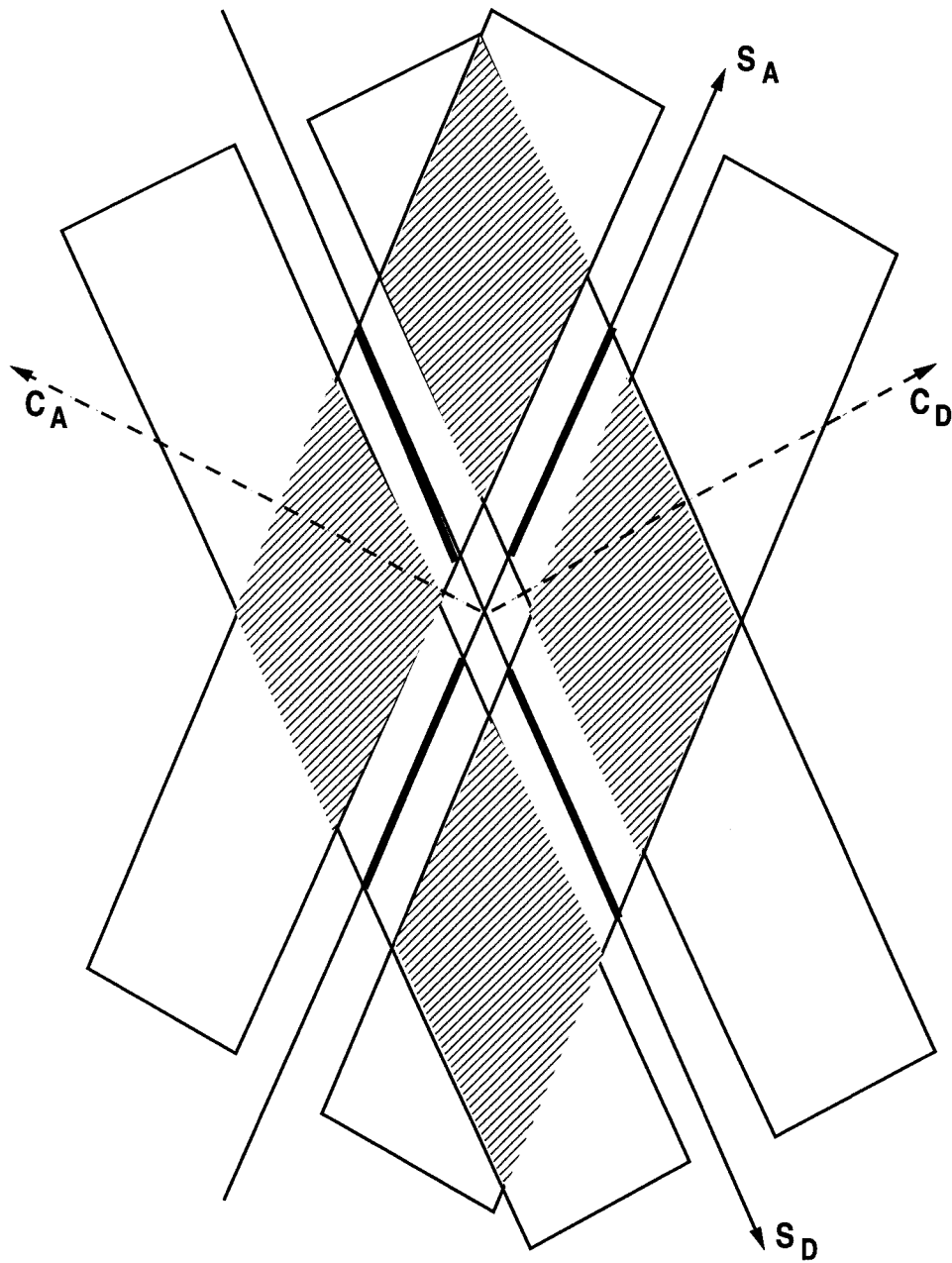


Figure 7:

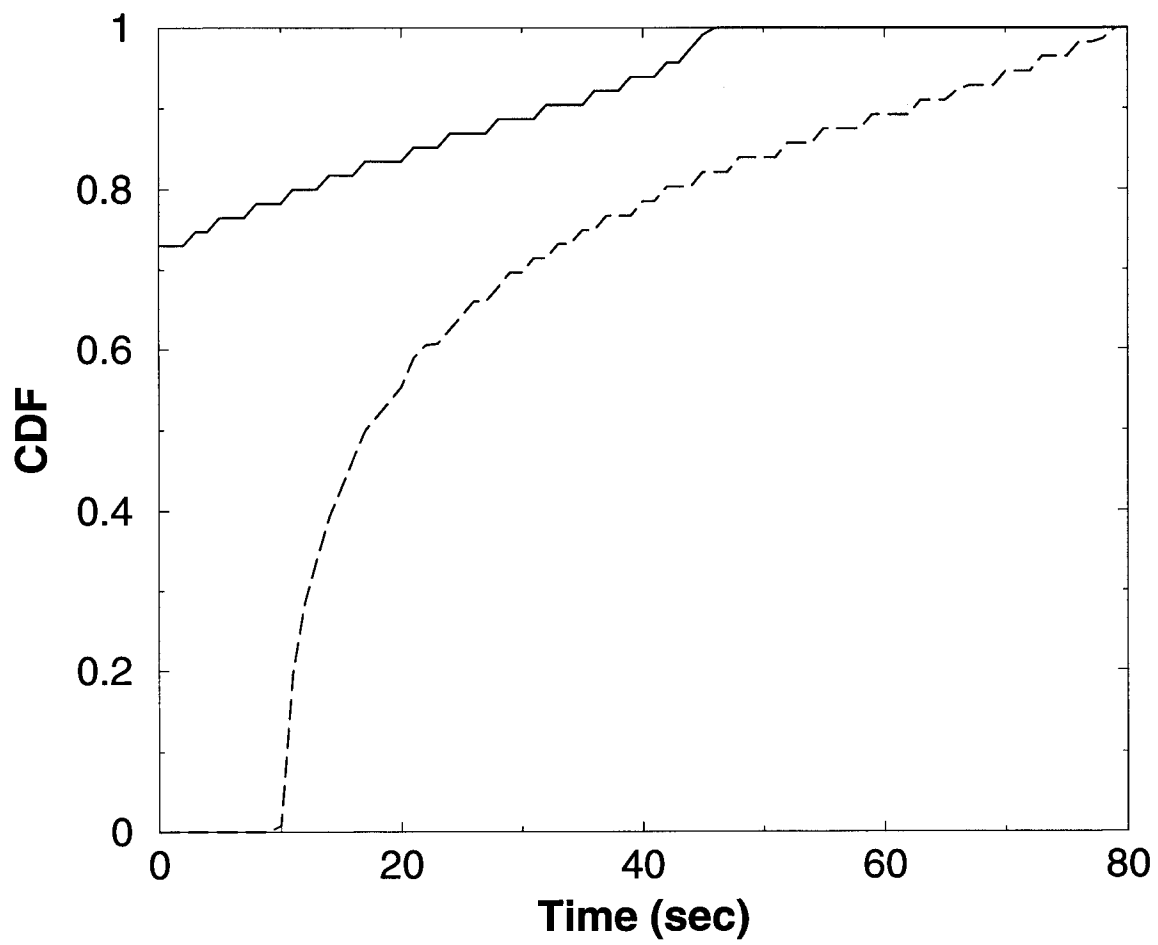


Figure 8:

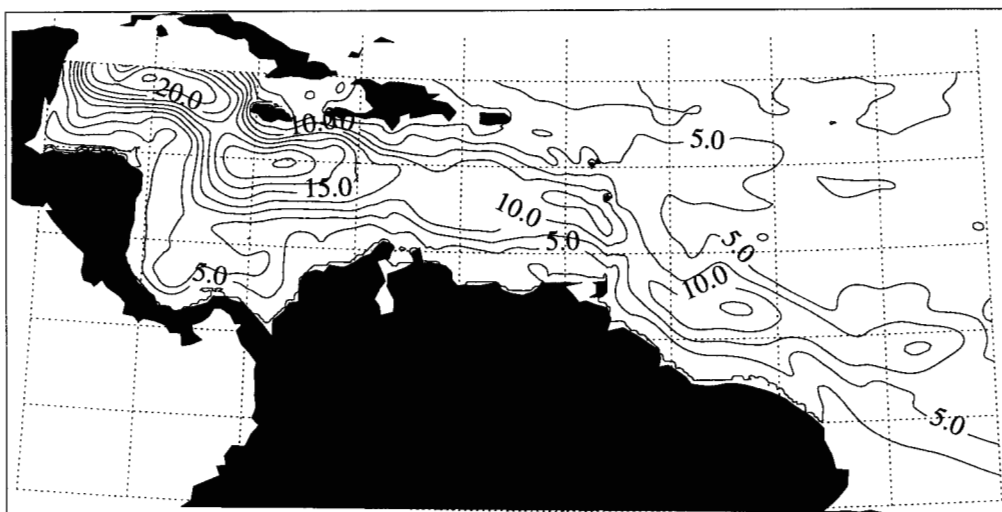


Figure 9:

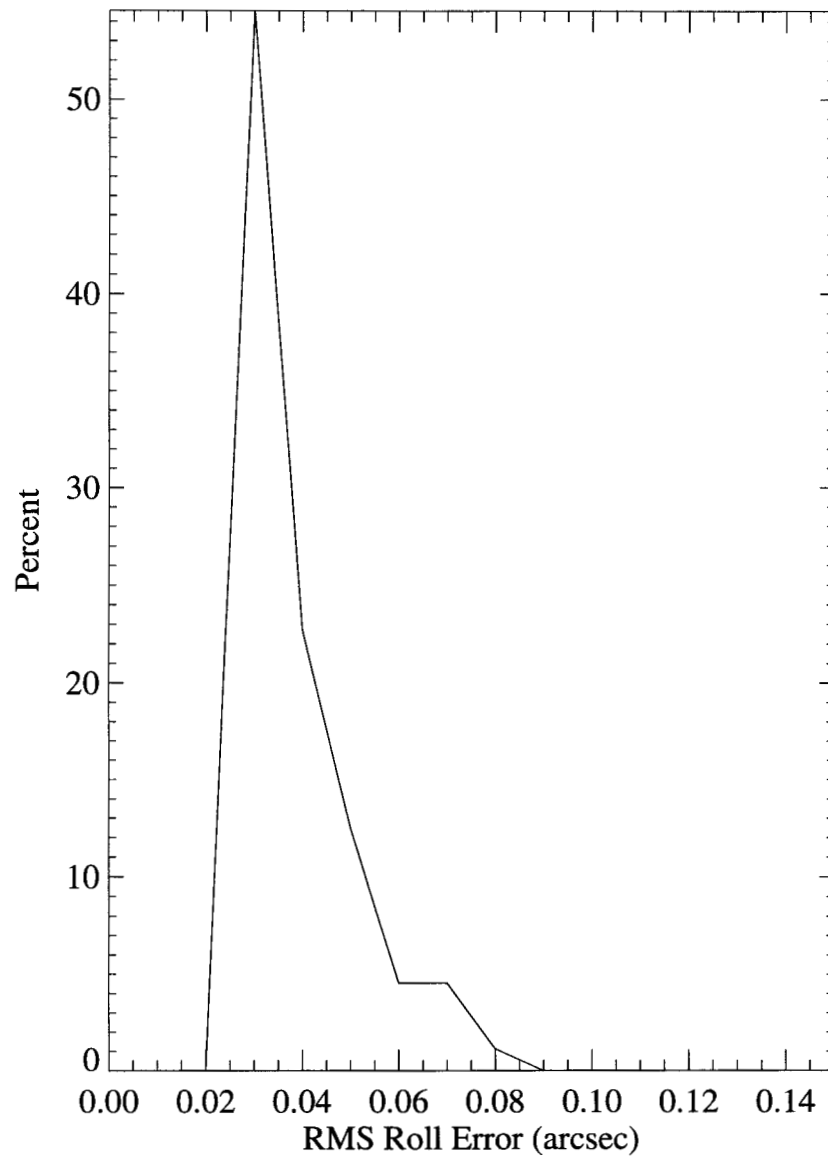


Figure 10:

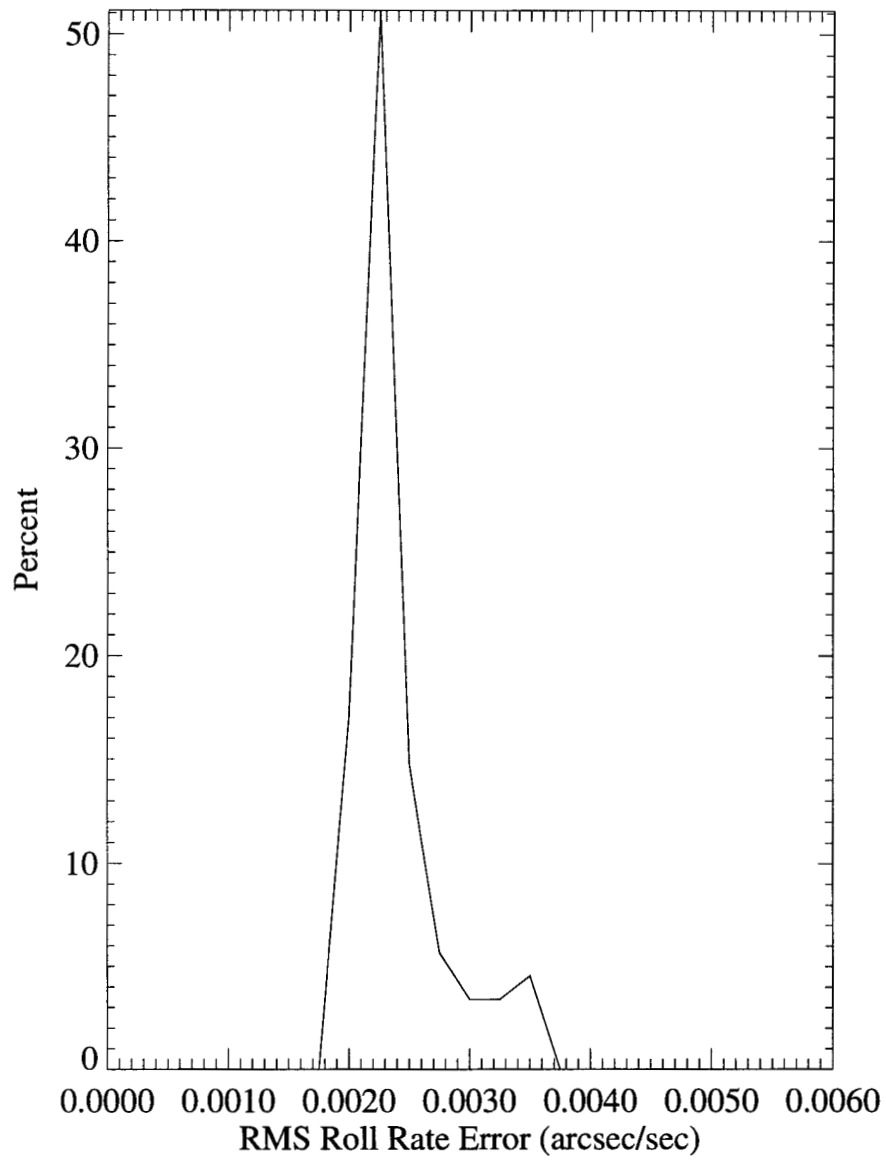


Figure 11:

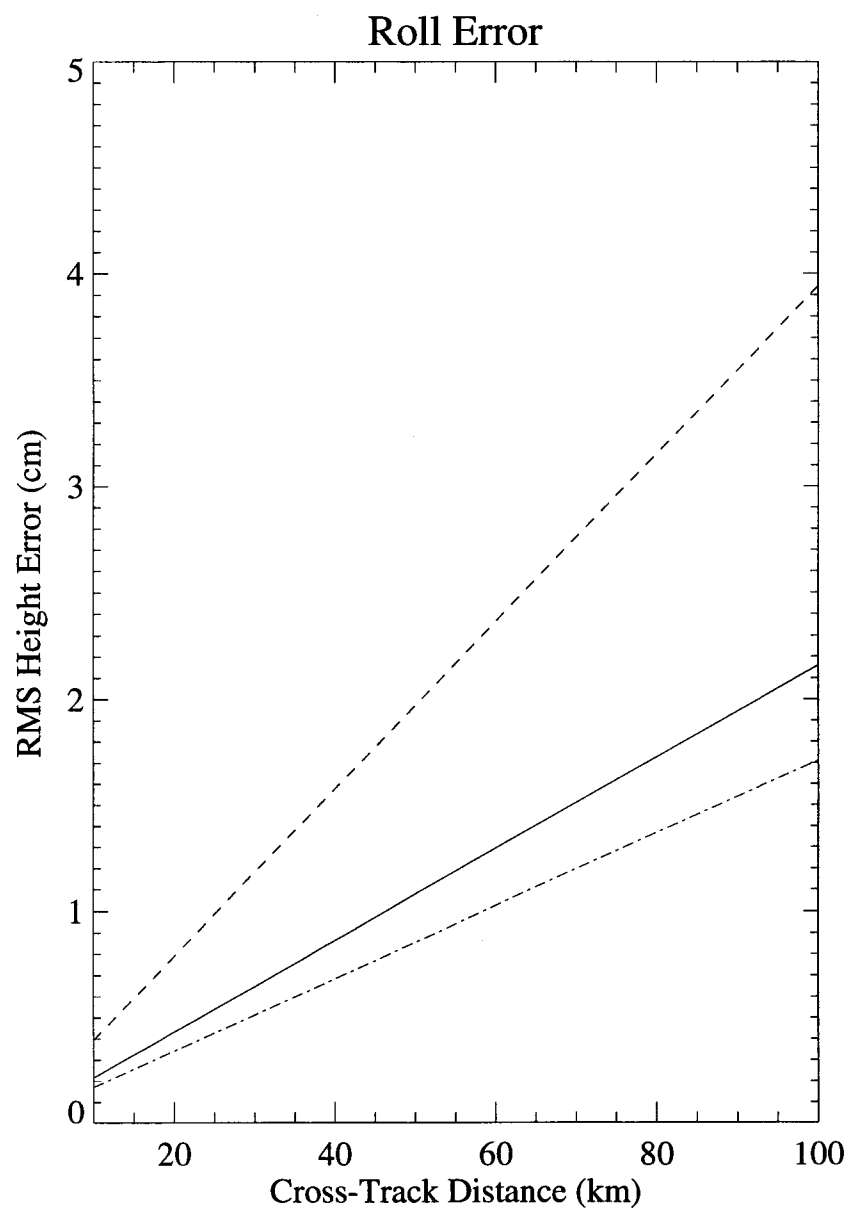


Figure 12:

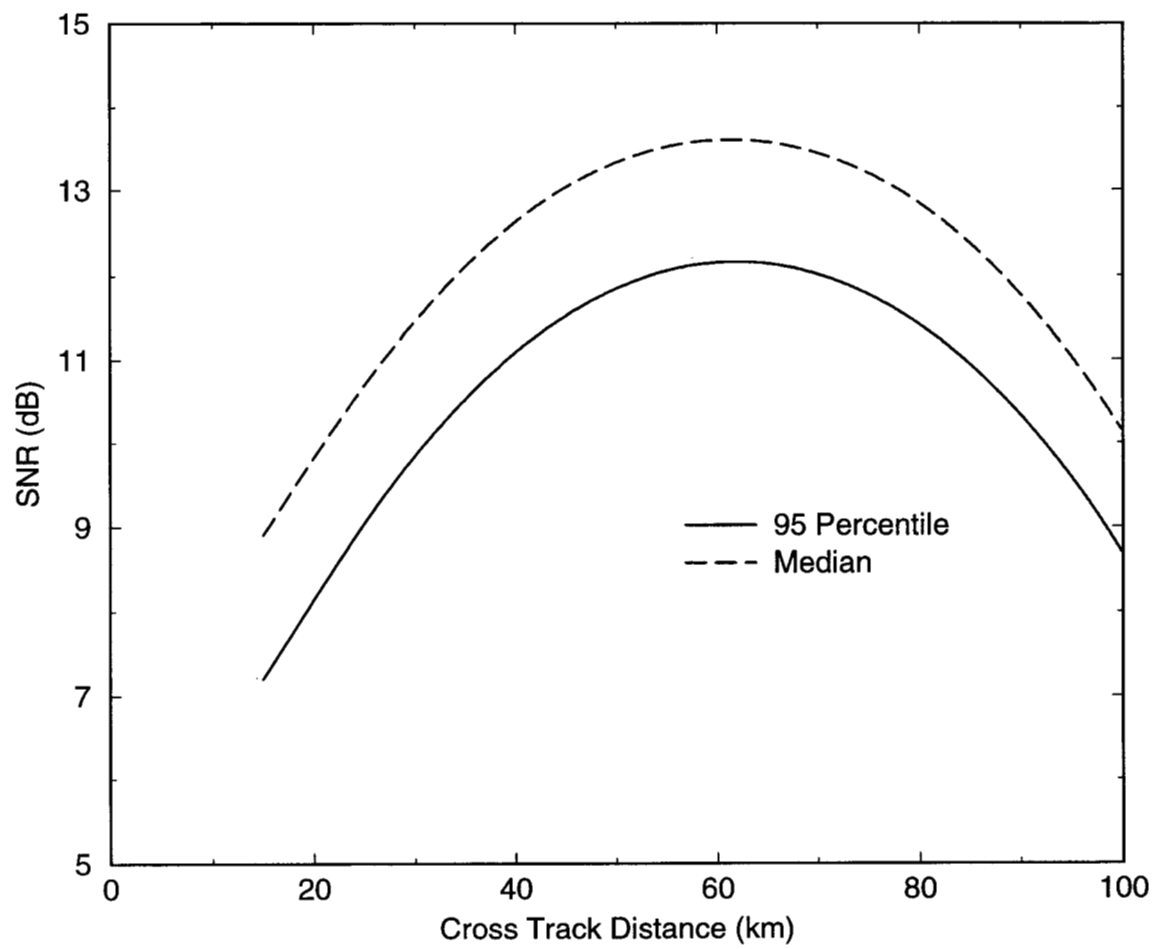


Figure 14:

Wide-Swath Altimeter Correlation

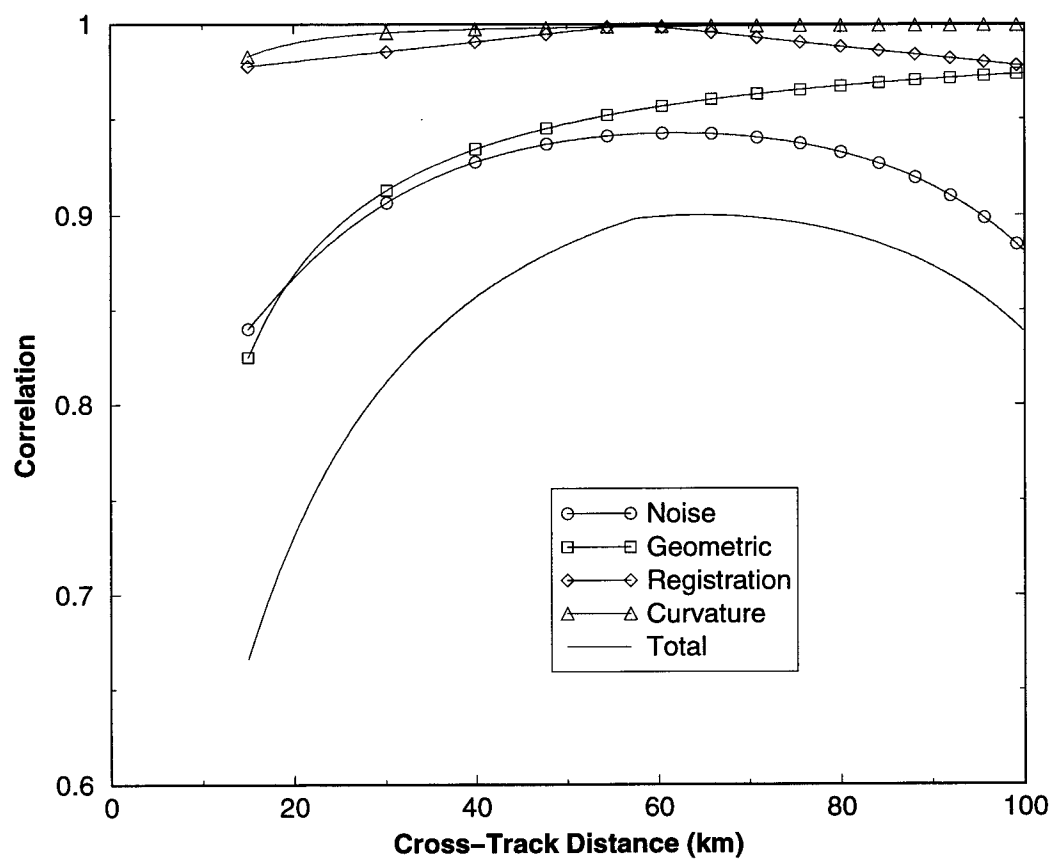


Figure 15:

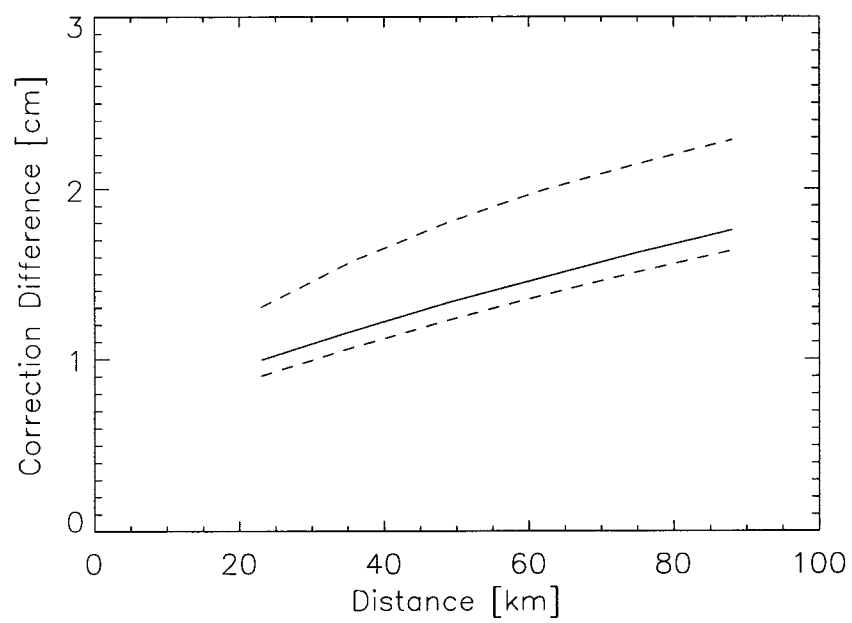


Figure 17: